

ANALYTICAL INVESTIGATION ON ROTATIONAL BEHAVIOR OF BEAM-COLUMN DOVETAIL JOINTS IN TRADITIONAL CHINESE TIMBER ARCHITECTURE

Zherui LI¹, Jianyang XUE², Akihisa KITAMORI³

ABSTRACT: In this study, we conducted a theoretical analysis of the rotational behavior of beam–column dovetail joints in traditional Chinese timber frames. By clarifying the moment generation mechanism and influence of rotational embedment yielding in timber perpendicular to the grain on joints rotational behavior, an analytical model for dovetail joints at the column head was developed. The asynchronous manifestation of rotational embedment deformation across the column surface, tenon cheeks, and upper and lower surfaces of the tenon head was examined, and the corresponding characteristic yield points and consequent reduction in rotational stiffness were derived in the model. The Inayama embedment theory was employed to clarify the effect of rotational embedment with varying end lengths on the movement of the joint rotation center and asymmetric moment generated in different rotational directions. The accuracy of the analytical model was validated through a comparative analysis by involving five sets of experimental data, for estimating the initial stiffness, post-yield stiffness, and identified yield points. The implications of the parameters, including the initial gap between the tenon and mortise, geometric dimensions of the dovetail tenon, and friction coefficient were discussed, and mutual verified with finite element analysis models.

KEYWORDS: Traditional timber structure, Dovetail joint, Mortise-and-tenon, Analytical model, Rotational embedment

1 – INTRODUCTION

Known as one of the most widely used traditional timber connections in the world, dovetail joint can provide good tensile resistance due to its angled shape of its mortise and tenon. In China, the earliest application of dovetail joint in architecture can be traced back to Neolithic Age. By the 14th century, dovetail had become the main joint form for purlins extension and connections between beams and columns (Fig. 1) in the Palace-style timber frames [1].

In addition to the essential functions of interconnecting and stabilizing the column head, the dovetail beam-column joint also functions as a semi-rigid connection and provides a discernible rotational moment. Therefore, the hysteretic behavior of the beam-column dovetail joints had been studied experimentally [2-6], including various parameters, such as the gap between the tenon and mortise, geometric dimensions of the tenon, size effect, friction coefficient, and their effect on the rotational behavior of dovetail joints. Conclusions drawn from above investigations revealed

common damage patterns for the beam-column dovetail joint, including the withdrawal of the dovetail tenon, partial embedment of the upper and lower edges of the dovetail and column surface, and transverse fracture of wood fibers at the mortise.

In prevailing analytical model of dovetail joints between beam and column, moment resistance arises from the compression and friction at the interface between the tenon cheek and mortise is highlighted [6,7]. However, simplifying assumptions for timber material characteristics and joint deformation led to determining the joint rotation center as either the centerline or the edge of the beam in relevant calculations. This resulted in notable discrepancies even within the elastic deformation stage compared to actual mechanical behavior. Based on experimental and finite element method (FEM) simulation [2, 6, 8], the actual joint rotation center lies between the beam centerline and edge. This position is strongly affected by the compression of the beam end against the column. Significant variations in the

¹ Zherui LI, College of Civil Engineering, Xi'an University of Architecture and Technology, Xi'an, China, lzh_6527@163.com

² Jianyang XUE, College of Civil Engineering, Xi'an University of Architecture and Technology, Xi'an, China.

³ Akihisa KITAMORI, Faculty of Engineering, Osaka Sangyo University, Osaka, Japan.

embedment length on the column surface before and after the yield point influenced the position of the rotation center considering the lower yield strength of the timber perpendicular to the grain and its rapid stiffness reduction after yielding. This has a significant effect on the stress distribution along the tenon cheeks. In addition, Chun *et al.* [9] also pointed out that the pull-out deformation of a dovetail tenon with shoulders is greater than that without shoulders at the same rotation angle. This phenomenon reflects that the compression of tenon shoulders at beam end has significant impact on the joint rotation center. Moreover, Yu *et al.* [10] indicated that the moment of dovetail beam-column joints manifests a certain degree of asymmetry in the positive and negative rotation directions, which is in concert with experimental observations [4, 5].

This study introduces an analytical model designed to assess the moment resistance of beam-column dovetail joint. Asymmetrical moments resulting from variations in the rotational embedment of the column surface in the positive and negative rotation directions are considered; the effect of asynchronous yielding at the column and dovetail cheeks on the deviation of the rotation center and reduction in stiffness during the elastoplastic stage is investigated. The accuracy of the analytical model was validated through comparative analysis with experimental data across diverse parameter sets.

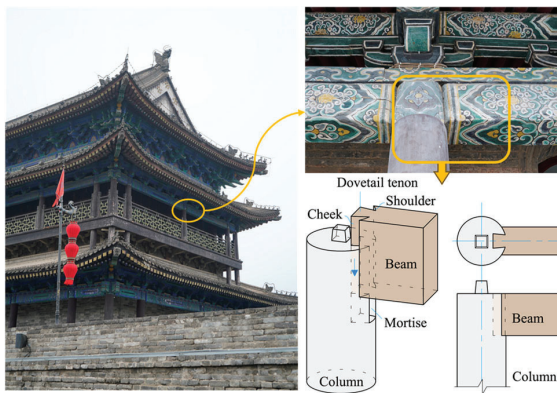


Figure 1. Typical beam-column dovetail joints in traditional Chinese timber frames

2 – ANALYTICAL INVESTIGATION

2.1 BASIC ASSUMPTIONS

The following assumptions were considered.

1) When subjected to lateral forces, the deformation of a timber frame is shown in Fig. 2. The column rocking behavior induces the elevation of the upper cap beams, and the vertical load carried by the cap beam was predominantly transmitted to the column. Therefore, we

posit that the alignment between the beam and cap beam remains approximately parallel. Only the relative rotation between the column and beam is considered in the model, and the constraint imposed by the cap beam on the rotation of the beam-column connection is neglected.

2) With the columns and beams serving as load-bearing components, only the deformation and damage localized at the mortise-tenon joint areas were considered in the model. The flexural and shear deformations inherent to the columns and beams were omitted from the analysis.

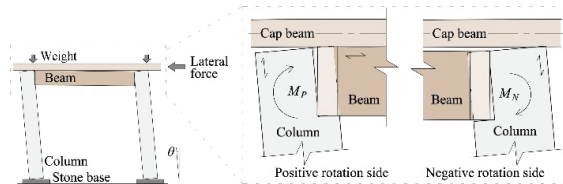


Figure 2. Local deformation of beam-column joints in the frame subjected to lateral force.

3) The analysis excludes the consideration of compressive deformation parallel to the grain because of the difference between the elastic modulus and compressive strength of timber parallel to the grain compared with those perpendicular to the grain.

4) Based on experimental observations [2-9] of the typical failure characteristics of dovetail beam-column joints, the primary deformations considered in the analysis include embedment perpendicular to the grain at the tenon cheeks and corresponding mortise; embedment on the upper and lower surfaces of the dovetail tenon, embedment on the surface of the column; and tensile splitting of the mortise perpendicular to the grain.

5) The calculation of reaction forces under partial rotational compression was based on the Inayama embedment model [11], as illustrated in Fig. 3. This model considers the resultant force, comprising the reaction of the loading area N_p , and the reaction of the end area along the x- and y-axes (N_{x1} , N_{y1} , and N_{y2}) as given in (1)-(5), respectively. Meanwhile, the ratio of the compressive modulus of elasticity ($E_0/E_{90}=29.2$) and characteristic value ($\gamma=3/Z_0$) defined in the model refer to the amendment proposal of E_{90} and γ under the rotational embedment mode, as recommended by Kitamori *et al.* [12]. In the elastic stage, the combined action points of forces N_p , N_{y1} , and N_{y2} are located at $2/3$ of the loading length x_p from the rotation center, whereas N_{x1} acts at x_p from the rotation center. Therefore, the rotational embedment moment is obtained in (6). Yield rotation angle θ_y is given in (7), and the stiffness after yielding in the elastoplastic stage decreases to approximately $1/6$ to $1/10$ of the initial stiffness [13].

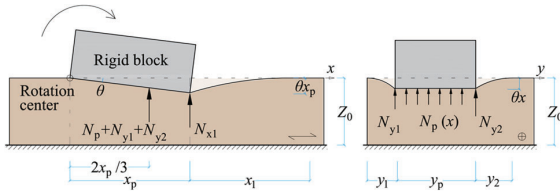


Figure 3. Sectional view of the reaction forces of timber under rotational embedment [11].

The resultant reaction force ΣN determined according to the Inayama embedment model is:

$$\Sigma N = N_p + N_{y1} + N_{y2} + N_{x1} \quad (1)$$

where the reaction of the loading area is:

$$N_p = \int_0^{x_p} N_p(x) dx = \frac{x_p^2 y_p E_{90} \theta}{2Z_0} \quad (2)$$

The reactions of the end area along the x and y axes are:

$$N_{y1} = \frac{1}{\gamma^{ny} y_p} (1 - e^{-\gamma^{ny} y_1}) \cdot N_p \quad (3)$$

$$N_{y2} = \frac{1}{\gamma^{ny} y_p} (1 - e^{-\gamma^{ny} y_2}) \cdot N_p \quad (4)$$

$$N_{x1} = \frac{2}{\gamma^{nx} x_p} (1 - e^{-\gamma^{nx} x_1}) \cdot N_p C_y \quad (5)$$

$$\Sigma M = K_\theta \cdot \theta = \frac{x_p^3 y_p E_{90} C_y}{Z_0} \left[\frac{1}{3} + \frac{Z_0}{3x_p} \left(1 - e^{-\frac{3x_1}{Z_0}} \right) \right] \cdot \theta \quad (6)$$

$$\theta_y = \frac{Z_0 f_m}{x_p E_{90} \sqrt{C_x C_y C_{xm} C_{ym}}} \quad (7)$$

In (2)-(7), x_p and y_p represent loading lengths parallel and perpendicular to the grain, respectively; x_1 represents the end length parallel to the grain direction; y_1 and y_2 represent the end lengths perpendicular to the grain direction; C_x represents the stiffness increasing factor parallel to the grain, calculated as $C_x = 1 + \frac{1}{\gamma^{nx} x_p} (1 - e^{-\gamma^{nx} x_1})$; C_y represents the stiffness increasing factor perpendicular to the grain, calculated as $C_y = 1 + \frac{1}{\gamma^{ny} y_p} (2 - e^{-\gamma^{ny} y_1} - e^{-\gamma^{ny} y_2})$; and n represents a substitutional coefficient between the direction parallel and perpendicular to the grain, which varies from 5 to 7 according to the wood species. In addition, $C_{xm} = 1 + \frac{2}{\gamma^{nx} x_p}$, $C_{ym} = 1 + \frac{2}{\gamma^{ny} y_p}$, $f_m = 0.8f_{cv}$, where f_{cv} represents the standard embedment yield stress of partial compression perpendicular to the grain.

2.2 GEOMETRIC CONDITIONS DURING ROTATION

When the beam-column dovetail joint undergoes a rotation angle θ , with O as the rotation center, the dovetail joint head manifests an outward displacement δ_i , whereas the

opposing end of the joint moves toward the column (Fig. 4). This action induces compression on the column surface by the shoulders of the dovetail joint, specifically at the beam end, which results in a rotational embedment deformation δ_e influenced by the excess embedment length x_1 , tending toward infinity and zero as the dovetail joint rotated in the positive and negative directions, respectively. Consequently, the reaction force N_b experiences variations, signifying that the force equilibrium relationship of the dovetail joint and the position of the rotation center are altered accordingly. Hence, the beam-column dovetail joint manifested a discernible asymmetry in the rotational performance in the positive and negative directions. It should be noted that, in the actual fabrication process of dovetail joints, the tenon length l is usually controlled to be slightly smaller than the mortise length to ensure a tight fit between the tenon shoulder and the column. Especially in the presence of tenon shoulders, the compressive area of the tenon shoulder is significantly larger than that of the front edge of the tenon during rotation. Therefore, the potential compressive effect of the front edge of the tenon is ignored in the analysis.

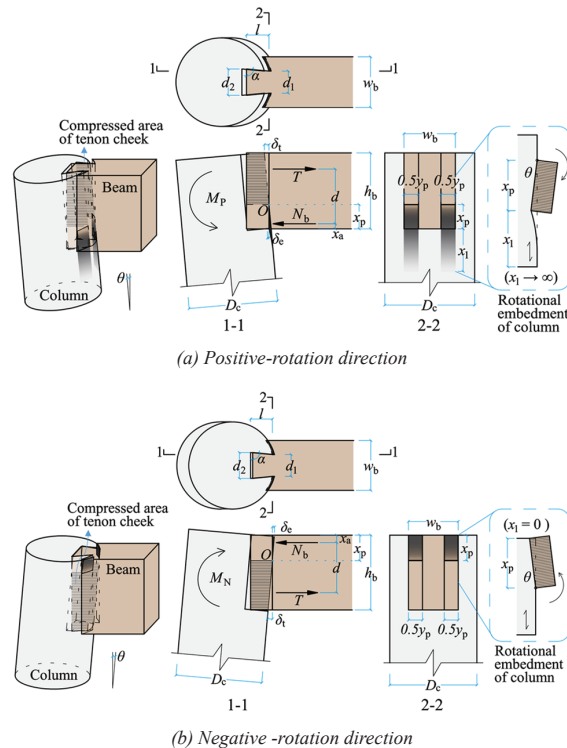


Figure 4. Deformation and internal force distribution of beam-column dovetail joint.

A compressive deformation e transpires between the mortise and tenon cheek during the tenon extraction process because of the trapezoidal configuration of the

dovetail tenon (Fig. 5(a)). Given that both the contact surfaces of the mortise and tenon cheek sustain compression perpendicular to the grain, half of the deformation $e/2$ occurs on each of these surfaces. Throughout the rotational movement of the dovetail joint, the compressive deformation along the tenon cheek progressively increases from the rotation center, thereby corresponding to deformation angle θ_c (Fig. 5(b)). The deformation at equivalent levels can be approximated as a rectangular distribution. The embedment deformation leads to a compressive internal force N_t perpendicular to the tenon cheek along with the corresponding friction μN_t , to resist the tensile force T . The relationships among δ_t , e , θ_c , and global rotation angle θ are given in (8)-(10). The thickness d_2 and d_1' of the tenon head corresponding to the compressed surface of the tenon cheek exhibit notable proximity when the inclination angle α in the beam-column dovetail joint typically exceeds 80° . Consequently, the strain at the same height on the tenon cheek followed a rectangular distribution. The relationship between the maximal compressive strain ε_{em} for the two tenon cheeks and embedment deformation e is given in (11).

$$\delta_t = (h_b - x_p) \cdot \theta \quad (8)$$

$$e = \delta_t \cdot \cos \alpha \quad (9)$$

$$\theta_c = \frac{1}{2} \cos \alpha \cdot \theta \quad (10)$$

$$\varepsilon_{em} = \frac{2e}{d_2 + d_1'} = \frac{2\delta_t \cos \alpha}{d_2 + d_1' + 2\delta_t \cot \alpha} \quad (11)$$

In (8)-(11), where h_b represents the beam height, x_p represents the embedment length of the beam end, and d_1 and d_2 represent the tail and head thicknesses of the dovetail tenon, ε_{em} represents the maximal compressive strain of the tenon cheeks, corresponding to embedment deformation e , respectively.

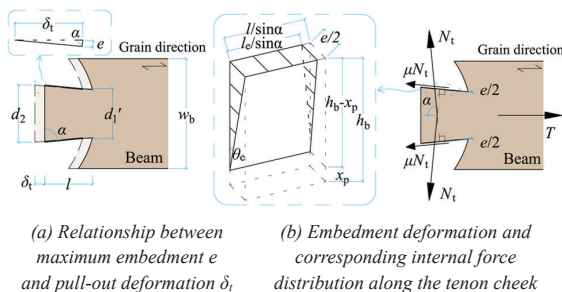


Figure 5. Pull-out deformation and internal force distribution at the tenon cheek.

2.3 INTERNAL FORCE EQUILIBRIUM

Elastic stage

Based on the deformation relationships and internal force distributions depicted in Fig. 4, the tensile force T induced by the dovetail tenon and compressive force N_b originating from the beam end to the column are equivalent.

$$T = N_b \quad (12)$$

where N_b represents the resultant force of the rotational embedment perpendicular to the grain. The position of N_b is identified as x_a from the beam edge, as shown in (13) and (14), respectively.

$$N_b = \frac{x_p^2 \gamma_p C_y E_{90}}{2Z_0} \left[1 + \frac{2Z_0}{3x_p} \left(1 - e^{-\frac{3x_1}{Z_0}} \right) \right] \cdot \theta \quad (13)$$

$$x_a = \frac{x_p}{3C_x} \quad (14)$$

In (13) and (14), N_b is obtained by substituting these parameters into (1)-(5) with $E_{90} = \frac{E_0}{29.2}$ and $\gamma = \frac{3}{Z_0}$. Stiffness increasing factors C_x and C_y are given by (15) and (16). Considering the practicality of the column section being circular in Chinese traditional timber frames, Z_0 is converted to the side length of a rectangle equivalent in area to the column section, shown in (17).

$$C_x = 1 + \frac{Z_0}{3x_p} \left(1 - e^{-\frac{3x_1}{Z_0}} \right) \quad (15)$$

$$C_y = 1 + \frac{Z_0}{3m_y p} \left(2 - e^{-\frac{3m_y 1}{Z_0}} - e^{-\frac{3m_y 2}{Z_0}} \right) \quad (16)$$

$$Z_0 = \sqrt{\frac{\pi D_c^2}{4}} \quad (17)$$

In the positive-rotation direction (i.e., $x_1 \rightarrow \infty$), N_b and x_a are given as

$$N_b = \frac{x_p^2 \gamma_p C_y E_{90}}{2Z_0} \left(1 + \frac{2Z_0}{3x_p} \right) \cdot \theta \quad (18)$$

$$x_a = \frac{x_p}{3 \left(1 + \frac{2Z_0}{3x_p} \right)} \quad (19)$$

In the negative-rotation direction ($x_1 = 0$), N_b and x_a are given by

$$N_b = \frac{x_p^2 \gamma_p C_y E_{90}}{2Z_0} \cdot \theta \quad (20)$$

$$x_a = \frac{x_p}{3} \quad (21)$$

Based on the deformation and internal force distributions depicted in Fig. 5, the relationship between tensile force T

and compressive force N_t generated on the tenon cheeks is given by (22). Here, N_t can be determined by integrating the compressive stress across the surface of the two tenon cheeks, as given in (23). In the elastic stage, the stress distribution along the tenon cheek aligns with the associated strain (Fig. 6(a)). On the pull-out side of the dovetail tenon, the corresponding maximal compressive stress perpendicular to the grain is denoted as σ_{em} .

$$T = 2(\cos \alpha + \mu \sin \alpha) N_t \quad (22)$$

$$N_t = \int \sigma_c = \frac{(h_b - x_p)^2 (l + 2l_e) E_{90} \cos \alpha}{3 \sin \alpha (d_1' + d_2)} \cdot \theta \quad (23)$$

In (22) and (23), μ represents the friction coefficient between the mortise and tenon, varying from 0.3–0.5 [13], l represents the length of dovetail tenon, and l_e represents the compressed projection length of the tenon cheek corresponding to the maximal compressive strain ε_{em} . Further, the relationship between σ_{em} and ε_{em} follows Hooke's law, i.e., $\sigma_{em} = E_{90} \cdot \varepsilon_{em}$.

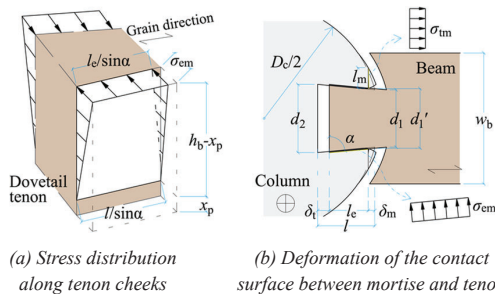


Figure 6. Deformation and stress distribution of the contact surface between mortise and tenon.

Considering that the tensile strength of timber perpendicular to the grain is only 1/40–1/30 of which parallel to the grain, the maximal tensile stress (σ_{tm}) at outer edge of the mortise in a column with a circular cross-section is prone to reach the transversal tensile limit (f_{90}), exhibiting fractures perpendicular to the grain under the tensile force exerted by the tenon (Fig. 6(b)). Therefore, besides deducting the tenon extraction length δ_t from the total tenon length l , when calculating l_e , a reduction of length δ_m corresponding to the tensile failure at the mortise is also necessary. Further, δ_m can be determined through the stress equilibrium and geometric deformation relationships between the dovetail tenon and mortise, given in (24)–(26).

$$l_e = l - \delta_t - \delta_m \quad (24)$$

$$\delta_m = \sqrt{\left(\frac{D_c}{2}\right)^2 - \left(\frac{d_1}{2}\right)^2} - \sqrt{\left(\frac{D_c}{2}\right)^2 - \left(l_m + \frac{d_1}{2}\right)^2} \quad (25)$$

$$l_m = \frac{\sigma_{em} l_e}{f_{90} \sin \alpha} (\cos \alpha + \mu \sin \alpha) \quad (26)$$

where (24) and (25) can be reformulated as a quadratic equation with respect to the variable δ_m . If ordering factors A, B, C_1, C_2, D as (27)–(31), then δ_m can be expressed as (32). l_m represents the transversal tensile splitting length at the mortise when the maximal tensile stress σ_{tm} reaches tensile strength f_{90} perpendicular to the grain.

$$A = 1 + C_2^2 \quad (27)$$

$$B = [2C_2^2(\delta_t - l) - 2C_1 - d_1' C_2] \quad (28)$$

$$C_1 = \sqrt{\left(\frac{D_c}{2}\right)^2 - \left(\frac{d_1}{2}\right)^2} \quad (29)$$

$$C_2 = \frac{(\cos \alpha + \mu \sin \alpha) \cdot \sigma_{em}}{\sin \alpha f_{90}} \quad (30)$$

$$D = C_1^2 + [C_2(l - \delta_t) + \frac{d_1'}{2}]^2 - \frac{D_c^2}{4} \quad (31)$$

$$\delta_m = \frac{-B - \sqrt{B^2 - 4AD}}{2A} \quad (32)$$

From (12)–(14) and (22)–(26), both N_b and N_t can be formulated as functions of the rotation angle θ and compressed length x_p of the beam end. Solving the equations relating N_b, N_t , and T , makes it feasible to deduce the values of x_p corresponding to distinct rotation angles during the elastic stage. Subsequently, the position of the rotation center can be determined, and the moment-rotation relationships for the beam-column dovetail joint in the positive (M_p) and negative (M_N) directions, are expressed by (33) and (34), respectively.

$$M_p = K_{p0} \cdot \theta = \frac{x_p^2 y_p C_y E_{90}}{3Z_0} \left(h_b + \frac{2Z_0 h_b + Z_0 x_p}{3x_p} \right) \cdot \theta \quad (33)$$

$$M_N = K_{N0} \cdot \theta = \frac{x_p^2 y_p C_y E_{90} h_b}{3Z_0} \cdot \theta \quad (34)$$

Elastoplastic stage

Based on the analyses of formation mechanism of the rotational moments M_p and M_N , it is known that the primary factors influencing the joint moment are the variations in compression forces N_t and N_b generated at the dovetail tenon and beam end. The rotational angles corresponding to the compressive yielding of the column surface and dovetail cheek exhibited asynchronous behavior, and N_b tended to yield prior to N_t . Consequently, a pivotal emphasis is placed on identifying the two distinctive points during the elastoplastic stage, θ_{y1} and θ_{y2} , associated with the yielding of N_b and N_t , respectively.

When the maximum compressive stress on the column surface reaches the embedment yield stress of timber perpendicular to the grain (f_{c90-c}), the associated yield rotation angle θ_{y1} can be derived directly following the

Inayama embedment model, as articulated in (7). As x_l approaches infinity and 0 in the positive and negative directions, respectively, C_x assumes respective values of C_{xm} and 1. Substituting the yield angle θ_{y1} into (33) and (34) enable the computation of the corresponding yield moments M_{Py1} and M_{Ny1} in the positive and negative directions, respectively, as shown in (35)-(38).

In the positive-rotation direction,

$$\theta_{y1} = \frac{Z_0 f_{c90-c}}{x_p E_{90} C_{xm} \sqrt{C_y C_{ym}}} \quad (35)$$

$$M_{Py1} = \frac{x_p^3 f_{c90-c} \left(h_b + \frac{2Z_0 h_b + Z_0 x_p}{3x_p} \right)}{3 C_{xm}} \cdot \sqrt{\frac{C_y}{C_{ym}}} \quad (36)$$

In the negative-rotation direction,

$$\theta_{y1} = \frac{Z_0 f_{c90-c}}{x_p E_{90} \sqrt{C_{xm} C_y C_{ym}}} \quad (37)$$

$$M_{Ny1} = \frac{x_p^3 f_{c90-c} h_b}{3} \cdot \sqrt{\frac{C_y}{C_{xm} C_{ym}}} \quad (38)$$

Assuming that the post-yield stiffness of N_b decreases to 1/8 of its initial value, the fundamental equilibrium relationship between N_b and T in (12) remains unaltered. Consequently, the compressed length x_p of the column surface undergoes a significant increase compared with the elastic deformation stage until the stress on the tenon cheeks reaches the compression yield strength perpendicular to the grain (f_{c90-b}). During the rotation process of the dovetail joint, the compression borne at the two tenon cheeks represents the rotational embedment with θ_e . Therefore, the yield rotation angle θ_{y2} is obtained by substituting (10) into (7), as shown in (39). Throughout this process, the equilibrium between T and N_t aligned with (21)-(26). Subsequently, the yielding moments M_{Py2} and M_{Ny2} in positive- and negative-rotation directions are derived by substituting θ_{y2} and solving for the corresponding x_p , as delineated in (40) and (41).

$$\theta_{y2} = \frac{(d_1 + d_2) f_{c90-b}}{2(h_b - x_p) E_{90} \cos \alpha \sqrt{\left[1 + \frac{(d_1 + d_2)}{6n(h_b - x_p)} \right] \left[1 + \frac{(d_1 + d_2) \sin \alpha}{2(l + 2l_e)} \right]}} \quad (39)$$

$$M_{Py2} = \frac{2f_{c90-b}(h_b - x_p)(l + 2l_e)(\cos \alpha + \mu \sin \alpha) \left(h_b + \frac{Z_0 x_p}{3x_p + 2Z_0} \right)}{9 \sin \alpha \sqrt{\left[1 + \frac{(d_1 + d_2)}{6n(h_b - x_p)} \right] \left[1 + \frac{(d_1 + d_2) \sin \alpha}{2(l + 2l_e)} \right]}} \quad (40)$$

$$M_{Ny2} = \frac{2f_{c90-b}(h_b - x_p)(l + 2l_e)(\cos \alpha + \mu \sin \alpha) h_b}{9 \sin \alpha \sqrt{\left[1 + \frac{(d_1 + d_2)}{6n(h_b - x_p)} \right] \left[1 + \frac{(d_1 + d_2) \sin \alpha}{2(l + 2l_e)} \right]}} \quad (41)$$

Fig. 7 expresses the stress distribution in the tenon cheek before and after yielding. As the maximum compression stress σ_{em} reached f_{c90-b} , the stress distribution along the

height direction of the tenon cheek transitions from a triangle to a trapezoid. Simultaneously, in correlation with the increase of δ_i , the embedment length l_e between the tenon cheek and mortise diminishes continually, i.e., the stress integration manifests a parabolic descent trend as θ increases above θ_{y2} . For computational simplicity, the stress distribution along the height direction of the tenon cheek can be assumed to be an intermediate state between the fully triangular and rectangular distributions under large rotation angles [14]. The distance between the reaction force T and the rotation center was considered $\frac{7}{12}(h_b - x_p)$. The critical rotation angle at this point is estimated to be approximately $2\theta_{y2}$ by inversely deducing the position of the centroid of this trapezoidal distribution. When $\theta_{y2} < \theta < 2\theta_{y2}$, the yielding of both N_b and N_t leads to a reduction in stiffness to 1/8 of their initial stage, and the distance between T and N_b diminishes progressively, causing the resultant moment to approximate stability. Upon surpassing $2\theta_{y2}$, the stress integration at the tenon cheek decreases rapidly with diminishing l_e . Until l_e decreases to 0, it signifies the disengagement of the outer edge of the tenon (θ_u). Substituting $l_e=0$ into (8) and (24), the ultimate rotation angle θ_u , and corresponding ultimate moment M_u in both positive- and negative-rotation directions can be determined by (42) and (43).

$$\theta_u = \frac{l - \delta_m}{h_b - x_p} \quad (42)$$

$$M_u = \frac{l}{l + 2l_e} \cdot M_{y2} \quad (43)$$

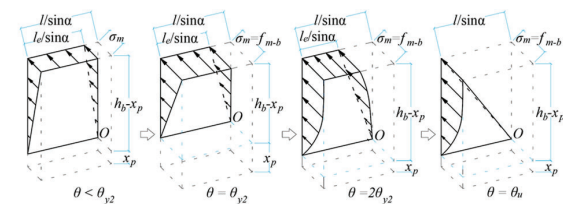


Figure 7. Stress distribution of the tenon cheek before and after yielding.

3 – MODEL VERIFICATION

3.1 COMPARISON WITH EXPERIMENTAL DATA

Firstly, a comparative analysis was conducted by juxtaposing five sets of experimental data sourced from different research teams [2-6] against the theoretical model. The density ρ and elastic modulus E_0 were used as references to facilitate a meaningful comparison, and other mechanical parameters derived by empirical equations [21]. In addition, E_{90} was taken as 1/29.2 of E_0 , f_{90} was taken as 1/30 of f_0 , and the friction coefficient μ of 0.4 was adopted between the tenon and the mortise.

Fig. 8a-8e illustrates a comparative analysis of the M - θ curves, which contrast with the estimations derived from analytical models with the experimental results. Experimental parameters varied across 9 samples as follows: density ρ ranged from 360–640 kg/m³, beam height h_b ranged from 150–240 mm, tenon length l ranged from 45–60 mm, and inclination angle of the dovetail tenon ranged from 83.7–85.2°. The effects of various boundary conditions in each experimental group were considered in the rotational moment simulations. The computed results exhibited a commendable concordance with the experimental data. The estimated initial stiffness, critical yield rotation angles, and post-yield stiffness associated with the embedment yield of the column surface and tenon cheeks aligned with the trends observed in the experimental data.

Composite relationships of M_p (M_N) and M' , which involve the effect of the initial sliding, are depicted in Fig. 8f. The characteristic rotation angles θ_{y1} , θ_{y2} , $\theta_{y'}$, and θ_u corresponding to the yield points and the ultimate moment were calculated according to the formulas in Section 2. An additional rotational moment M' is considered in Fig. 8d and 8e, due to the fixed boundary condition of upper surface of the dovetail tenon. The formation mechanism of M' was similar to that of a straight tenon (Nuki joint).

3.2 COMPARISON WITH FINITE ELEMENT MODEL

Anchoring the basic material properties and dimensional parameters in Ref. [2] as the control group (Case 0), the effect of the initial gap between the tenon and mortise, geometric dimensions of the dovetail tenon, and friction coefficient on the M_p (M_N)- θ curves of the dovetail joint were addressed individually [15]. The discernible trend reveals a substantial reduction of the initial stiffness K_0 and post-yield stiffness $K_{\theta 1}$ with an increase in e_0 . Furthermore, in comparison to the friction coefficient μ , the beam height h_b and tenon width d_2 showed a more significant effect on the initial and post-yield stiffness; the tenon length l predominantly affected the yield rotation angle θ_{y2} with an insignificant effect on the initial stiffness and θ_{y1} .

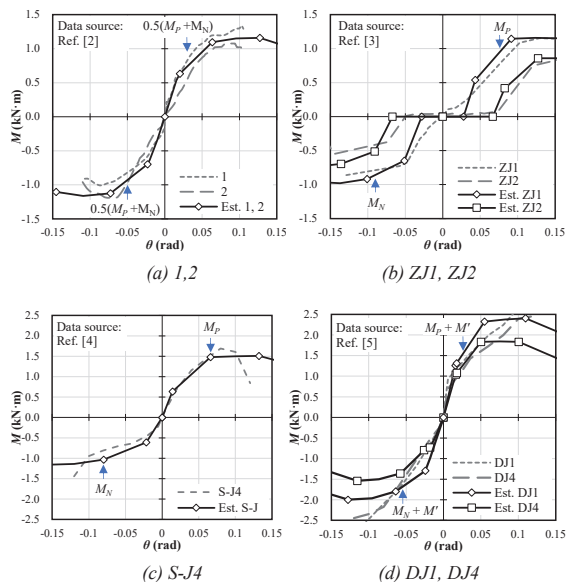
To further verify the accuracy of parametric analysis, a finite element analysis (FEA) model of single-bay frame corresponding to different parameter sets in Table 1 was established using Abaqus (Figs. 9, 10). Other fundamental dimensions and constraints of the frame model were also consistent with the experimental setup in Ref. [2]. Since the level of column top was slightly higher than the beam, and the upper mortise remained unfilled, thereby avoiding interference from the additional moment M' .

Since the dovetail joints at both ends of the beam generated M_p and M_N respectively under horizontal forces, the average of these two values was adopted for comparison with estimated results (Fig. 11). The variation trends of both initial stiffness and post-yield stiffness under different parameter influences align fundamentally with estimated results, which validates the accuracy of the analytical model. It should be noted that, when the gap e_0 between the tenon cheek and mortise was set to 0.5 mm, the unstable beam-column connection induced rigid-body rotation of the beam itself during the frame deformed under lateral force. This phenomenon resulted in more pronounced initial sliding angle and stiffness degradation in FEA simulations compared with calculated values.

4 – CONCLUSION

This study investigated the rotational behavior of beam-column dovetail joints in traditional timber frames. An analytical model of dovetail joints at both the column head and body, applicable to newly constructed buildings in traditional style, was formulated by elucidating the moment generation mechanism and effect of rotational embedment yielding in timber perpendicular to the grain on the rotational behavior of the joints.

The accuracy of analytical model was verified with existing experimental data, further discussions were conducted on the ramifications of the parameters including the initial gaps, geometric dimensions of the dovetail, and friction coefficient. Through comparative analysis with FEA models, it has been verified that the characteristic points obtained from the calculations can effectively reflect the influence of corresponding parameters.



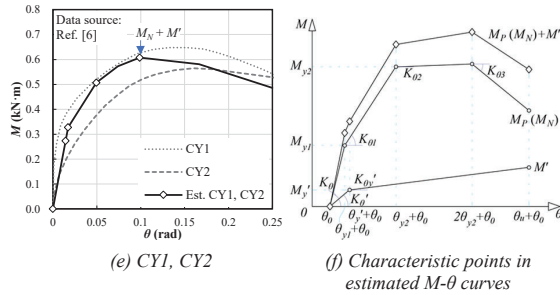


Figure 8. Comparison between estimations and experimental results.

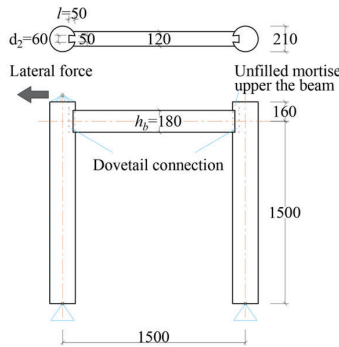


Figure 9. Size and constraint information of the single-bay frame model connected with dovetail joints.

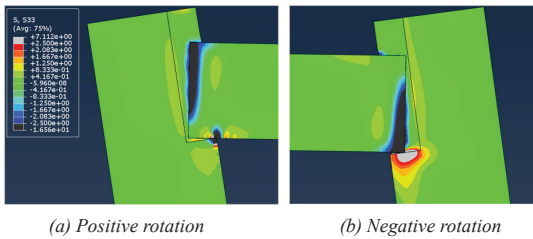


Figure 10. Typical stress distribution perpendicular to grain of the dovetail joint at 0.15 rad.

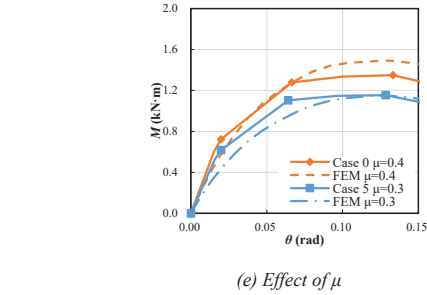
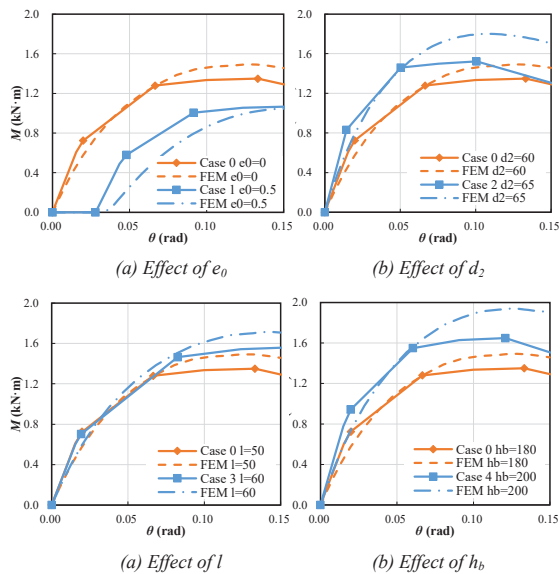


Figure 11. Comparison between estimations and FEA models.

Table 1: Estimated results of cases under different parameters.

Parameters/ characteristic values	Cases						
	0	1	2	3	4	5	
e_0 (mm)	0.0	0.5	0.0	0.0	0.0	0.0	
d_2 (mm)	60	60	65	60	60	60	
l (mm)	50	50	50	60	50	50	
h_b (mm)	180	180	180	180	200	180	
μ	0.4	0.4	0.4	0.4	0.4	0.3	
M_P	θ_{y1} (rad)	0.015	0.016	0.014	0.015	0.015	0.016
	θ_{y2} (rad)	0.067	0.064	0.050	0.083	0.060	0.064
	K_0 (kN·m/rad)	41.95	34.61	57.85	41.30	56.19	35.26
	K_{01} (kN·m/rad)	14.95	12.60	17.48	15.14	19.41	13.47
M_N	θ_{y1} (rad)	0.023	0.023	0.020	0.023	0.021	0.024
	θ_{y2} (rad)	0.077	0.073	0.057	0.097	0.069	0.073
	K_0 (kN·m/rad)	33.64	27.90	44.97	33.26	47.17	28.68
	K_{01} (kN·m/rad)	6.52	5.39	6.82	7.07	8.69	5.77

ACKNOWLEDGEMENT

This study is financially supported by National Natural Science Foundation of China (Grant-No. 52408210) and Shaanxi Province Postdoctoral Science Foundation, China (Grant-No. 2023BSHYDZZ143).

REFERENCES

[1] Liang S, Fairbank W. A pictorial history of Chinese architecture: a study of the development of its

- structural system and the evolution of its types, Mit Press, 1984.
- [2] Sui Y, Zhao H, Xue J, et al. Experimental study on characteristics of mortise-tenon joints in historic timber buildings. *World Earthquake Engineering*, 2010, 26(2): 88–92. (in Chinese)
- [3] Yao K, Zhao H, Ge H. Experimental studies on the characteristic of mortise-tenon joint in historic timber buildings. *Engineering Mechanics*, 2006, 23(10): 168–173. (in Chinese)
- [4] Xie Q, Du B, Xiang W, et al. Experimental study on seismic behavior and size effect of dovetail mortise-tenon joints of ancient timber buildings. *Journal of Building Structures* 2015, 36(3): 112–120. (in Chinese)
- [5] Li Y, Cao S, Xue J. Analysis on mechanical behavior of dovetail mortise-tenon joints with looseness in traditional timber buildings. *Structural Engineering and Mechanics*, 2016, 60(5): 903–921.
- [6] Chen C, Qiu H, Lu Y. Flexural behaviour of timber dovetail mortise-tenon joints. *Construction and Building Materials*, 2016, 112: 366–377.
- [7] Pan Y, Zhang Q, Wang X, et al. Research on mechanical model of dovetail joint for Chinese ancient timber structures. *Journal of Building Structures*, 2021, 42(8): 151–159. (in Chinese)
- [8] Gao Y. Experimental study and theoretical analysis of traditional timber typical mortise-tenon joints based on the wood friction mechanism and embedded pressure characteristics. Dissertation, Kunming University of Science and Technology, 2017. (in Chinese)
- [9] Chun Q, Pan J, Dong Y. Research on integrity damage indexes of the ancient timber frame buildings in the south China. *Science of Conservation and Archaeology* 2017, 29(6): 76–83. (in Chinese)
- [10] Yu P, Li T, Yang Q. Analytical model and rotational performance of dovetail mortise-tenon connection at the column head of traditional wooden frame. *Structures*, 2023, 57: 105256.
- [11] Inayama M. Study on Compression Perpendicular to the Grain in Wood, Part 4. *Proceeding of Architectural Institute of Japan (Kanto)*, 1993, pp 907–908 (In Japanese)
- [12] Kitamori A, Mori T, Kataoka Y, et al. Effect of additional length on partial compression perpendicular to the grain of wood. *J. Struct. Constr., AIJ*, 2009, 74(642): 1477–1485.
- [13] Architectural institute of Japan. *Design manual for engineered timber joints*. Maruzen publishing Co., Ltd., Tokyo, 2009, pp 252–257.
- [14] Murakami M, Kageyama M, Okamoto S. et al. Prediction and its verification on stiffness and bearing capacity of mud walls based on their lateral load carrying mechanism. *J. Struct. Constr. Eng., AIJ* 2006, 605: 119–126.
- [15] Li Z, Kitamori A, Zhang X, et al. Analytical investigation on the rotational behavior of dovetail mortise-tenon joints between beams and columns in traditional Chinese timber frames. *Journal of wood science*, 2024, 70: 50.